

Visualizing Correlations in the 2D Fermi-Hubbard Model with AI

Ehsan Khatami,^{1,*} Elmer Guardado-Sanchez,² Benjamin M. Spar,²
Juan Felipe Carrasquilla,³ Waseem S. Bakr,² and Richard T. Scalettar⁴

¹*Department of Physics and Astronomy, San José State University, San José, CA 95192, USA*

²*Department of Physics, Princeton University, Princeton, NJ 08544, USA*

³*Vector Institute, MaRS Centre, Toronto, Ontario, M5G 1M1, Canada*

⁴*Department of Physics, University of California, Davis, CA 95616, USA*

(Dated: April 20, 2022)

Strongly correlated phases of matter are often described in terms of straightforward electronic patterns. This has so far been the basis for studying the Fermi-Hubbard model realized with ultracold atoms. Here, we show that artificial intelligence (AI) can provide an unbiased alternative to this paradigm for phases with subtle, or even unknown, patterns. Long and short range spin correlations spontaneously emerge in filters of a convolutional neural network trained on snapshots of single atomic species. In the less well-understood strange metallic phase of the model, we find that a more complex network trained on snapshots of local moments produces an effective order parameter for the non-Fermi liquid behavior. Our technique can be employed to characterize correlations unique to other phases with no obvious order parameters or signatures in projective measurements, and has implications for science discovery through AI beyond strongly correlated systems.

Phases of strongly correlated electronic systems are often described in terms of straightforward patterns, which are theoretically understood using Landau symmetry-breaking theory [1]. For instance, ferromagnetism on a square lattice involves a uniform arrangement where the electrons' spins align and create a magnetic state with a wavevector $\mathbf{q} = \mathbf{0}$. Antiferromagnetism, slightly more complex, is revealed by a $\mathbf{q} = \pi$ alternation of the electrons' spin state on two sublattices. These choices, and incommensurate (spiral) order which bridges them at general \mathbf{q} , can be characterized in a unified way through the magnetic structure factor, $S(\mathbf{q})$, and further generalized to include time-domain patterns via the dynamic susceptibility, $\chi(\mathbf{q}, \omega)$. Similar statements apply to charge density wave and other phases involving diagonal long range order.

While many of our theoretical and experimental probes of interacting quantum systems have been constructed with coupling to these patterns in mind, there is an increasing realization that the most interesting strongly correlated phases might not be immediately accessible via such observables. Cuprate and iron-pnictide superconductors, which combine closely entwined conventional phases with well-established order parameters, and much less well-understood non-Fermi liquid (NFL) or pseudogap phases with so far 'hidden orders' are examples [2–4], as is the zoo of orbital ferromagnetism, superconductivity, and Mott insulating behavior in twisted bilayer graphene [5, 6]. The community of strongly correlated quantum systems is thus faced with the challenge of developing new means of identifying complex phases.

Here, we introduce an unbiased approach in which AI is used to extract hidden features from raw images of quantum many-body systems. We test our approach using projective measurements on a two-dimensional (2D) Fermi-Hubbard model, obtained through quantum gas

microscopy of ultracold fermionic atoms in an optical lattice. We find that filters of a convolutional neural network (CNN), trained to recognize snapshots of fermions, capture features at different densities that have clear interpretation in terms of short and long-range magnetic correlations. We further show that a more complex CNN can produce an effective order parameter for the NFL phase, based on the interplay of multiple types of density fluctuations, reflecting the more enigmatic nature of the correlations in this phase.

In the experiment, the 2D Fermi-Hubbard model is realized using a spin-balanced mixture of the first and third lowest energy states of ^6Li loaded into a square optical lattice. We work at a magnetic field of 615 G in the vicinity of the Feshbach resonance near 690 G, which gives us a scattering length of $1056(10) a_0$. The lattice depth is $7.25(2)E_R$, where E_R is the lattice recoil energy and $E_R/h = 14.66$ kHz. For these parameters we obtain $t/h = 850(20)$ Hz and $U/t = 8.0(1)$. Here, t and U are the nearest-neighbor hopping matrix element and the strength of onsite repulsive interaction, respectively, in the Hubbard model.

Using quantum gas microscopy techniques [7], we image the atoms in the lattice with single site resolution with a fidelity of 98%. When a fluorescence image is taken, atoms on doubly occupied sites undergo light assisted collisions and appear empty. An image taken this way allows us to extract the local moment on each site. Alternatively, we can apply a short pulse of resonant light prior to taking an image to eject atoms of one of the two hyperfine states. This allows us to measure the single component density of the remaining hyperfine state.

Our lattice beams produce a harmonic trapping potential, which if uncompensated leads to significant variations of the local density. To study regions of uniform density, we flatten the potential using light shaped using

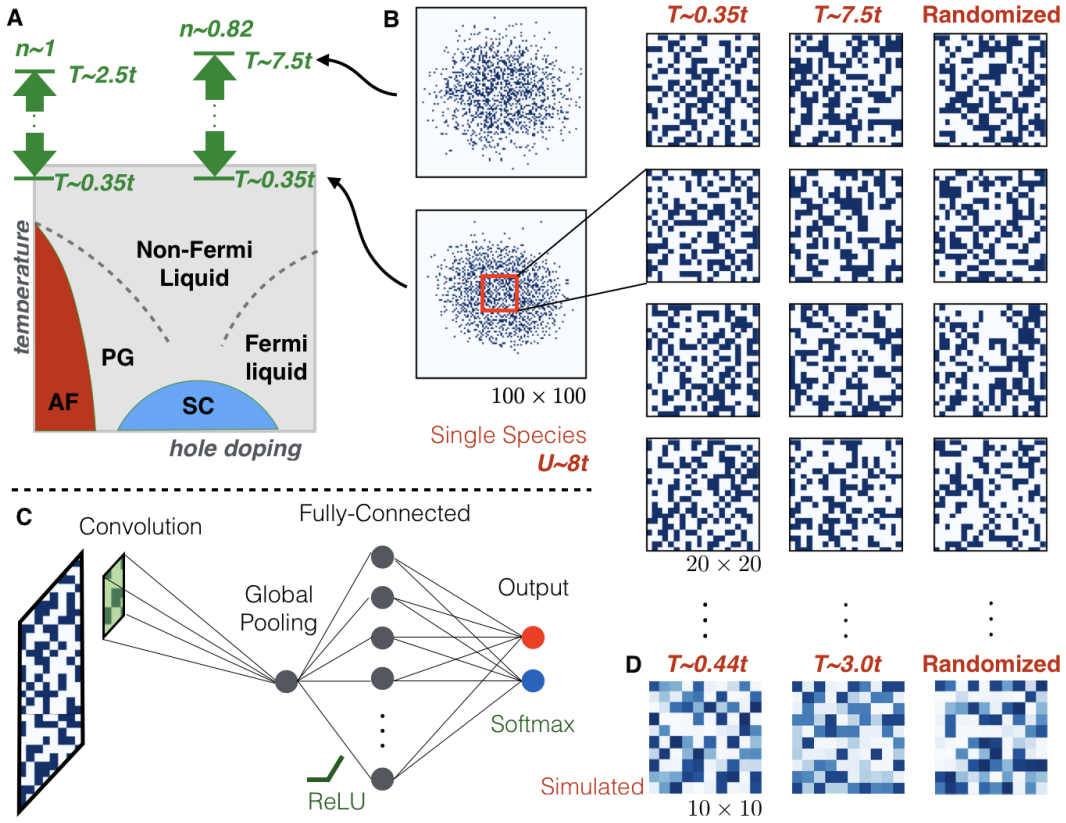


FIG. 1. **Phase diagram, sample snapshots, and CNN architecture.** (A) Schematic phase diagram of cuprate high-temperature superconductors in the space of temperature and hole doping. AF, PG and SC stand for antiferromagnetic, pseudogap, and superconducting phases, respectively. (B) Sample experimental snapshots taken at the density $n \sim 0.82$. Left: Two 100×100 -pixel samples of occupancy snapshots of a single species of fermions taken at $T \sim 0.35t$ (top panel) and $T \sim 7.5t$ (bottom panel). Blue pixels indicate a particle on a site. Right: The 20×20 -pixel center part of four randomly chosen snapshots at each of the extreme temperatures, along with four snapshots at the same density whose pixels have been randomly shuffled, i.e., “fake” snapshots. (C) The main convolutional neural network architecture used in this study. The architecture contains a convolutional layer with one filter and one feature map followed by a global pooling layer. The output of the pooling layer is fed to 8 fully-connected neurons, followed by an output softmax layer with two neurons, each associated with a temperature limit. We use the rectified linear unit (ReLU) as the activation function in all but the output layer. In our experiments we observe that the presence of the fully-connected layer accelerates the training of the neural network. (D) Sample 10×10 -pixel single-species snapshots from DQMC at two different temperatures along with one obtained by shuffling pixels of the snapshot at the lower temperature.

a spatial light modulator [8]. In the subsequent analysis, we work with a flattened region of 20×20 lattice sites.

Figure 1 shows several randomly chosen samples of binarized occupancy snapshots at an average density of $n = 0.82(2)$ at two extreme temperatures of $T \sim U$ and $T \sim 0.35t$ used in our study. These parameters place us within the NFL region of a typical cuprate phase diagram (Fig. 1A). Thermometry is performed using averages of various correlation functions taken over such snapshots [8].

The increasingly large number of snapshots taken in quantum gas microscope experiments in various regions of the parameter space lends itself to data-driven approaches for science discovery, such as the enlisting of AI. In fact, early implementations of machine learning techniques for the study of quantum many-body systems

demonstrated great potential [9–14]. Recent applications to experimental data have either directly led to the discovery of new physics [15–19] or the optimization of experimental processes [20, 21], including those related to quantum gas microscopy.

CNNs offer an ideal platform for the detection of patterns in the experimental snapshots. Not only can they efficiently compress the information in images and use them for classification, but also their trained filters provide a window into the relevant features observed [22]. Figure 1C shows the main CNN architecture we have used. After labeling them according to their temperature, hundreds of snapshots taken at the extreme temperatures along with their labels are provided to the CNN for training. During the training, the network adjusts its free parameters to minimize the difference between given

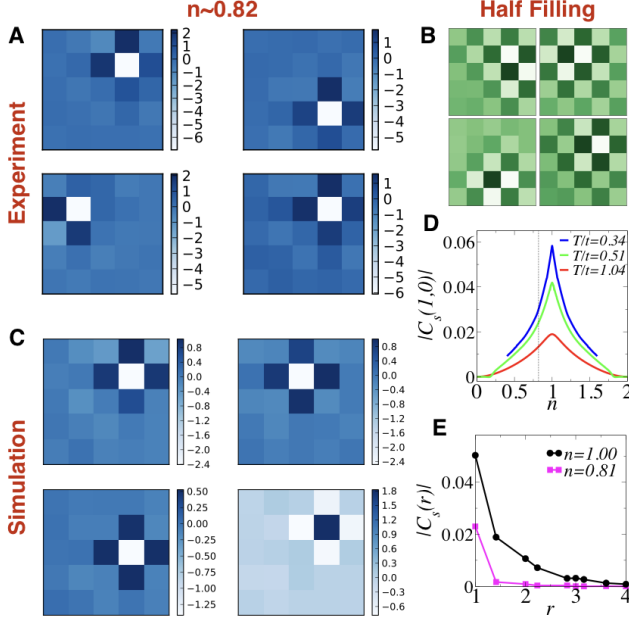


FIG. 2. **Analysis of single-species snapshots using CNNs with one filter.** Sample 5×5 filters for four independent runs are shown for (A) $n = 0.82$ and (B) $n \sim 1$. The CNN architecture is shown in Fig. 1C. The testing accuracies are between 91% and 95%. The visual pattern in each 5×5 filter in (A) is consistent with recognizing short range AF correlations. The four representative runs in (B) indicate patterns capturing long range order near half filling. (C) shows similar filters evolved from training runs using DQMC simulations. The testing accuracies are at least 68%. Panels (D) and (E) provide theory data for the nearest neighbor spin-spin correlation for $U = 8t$ vs. density at different temperatures (NLCE), and vs. distance for $n = 0.81$ and $n = 1.00$ at $T = 0.44t$ (DQMC). This figure illustrates that AI can capture the correct trends in magnetic behavior of the Hubbard model, and that the trained filters carry a clear physical interpretation.

labels and its prediction [23]. The convolutional layer in our CNN interacts directly with the input snapshots, and therefore, examining the filter after the completion of the training can teach us about the most important feature the network has picked up.

Figure 2A shows a sample of four 5×5 filters after four different runs in which the CNN is trained to distinguish experimental snapshots of a single species of fermions at the highest temperature from those at the lowest temperature when $n = 0.82$. If we expect mostly random behavior at high temperature, of the order of the largest energy scale in the system, the features that spontaneously develop in the filters during training will most likely represent patterns found in the low-temperature snapshots. We find that the CNN consistently makes the distinction with more than 91% accuracy, and it does so using filters showing a distinctive pattern indicative of short-range antiferromagnetic (AF) correlations. The nearest-

neighbor checkerboard pattern emerging in the filters is consistent with the fact that the correlation length in the NFL region is about one lattice spacing [24]. The appearance of this feature at different locations in the filter for different training runs points to a redundancy: on average the filter must reflect the translational symmetry of the underlying system.

Training the CNN using similar snapshots obtained near half filling results in filters that reflect a longer range anti-correlation between neighboring fermions of the same species (Fig. 2B). These findings suggest that the network effectively uses the strength of AF correlations as a measure for classifying snapshots of a single species of fermions. Figure 2, D and E show that the density, distance, and temperature dependence of the magnetic correlations of the model, $C_s(\mathbf{r})$ [23], which are calculated here on a 10×10 cluster using the determinantal quantum Monte Carlo (DQMC) [25], or in the thermodynamic limit using the numerical linked cluster expansion (NLCE) [26, 27], support this observation.

Quantum Monte Carlo simulations also provide a platform to corroborate these findings. However, except in one spatial dimension, these simulations cannot provide projective measurements in the density basis. Instead, theory “snapshots” can be constructed via expectation values of local charge or spin density using instances of auxiliary field variables during a simulation; for example, the i th pixel of a spin-up DQMC snapshot is $\langle \hat{n}_{i\uparrow} \rangle_h = 1 - \mathcal{G}_{ii\uparrow}(h)$, where $\mathcal{G}_{ii\uparrow}(h)$ is the i th diagonal element of the spin-up equal time Green’s function matrix for the auxiliary field instance h . We perform the simulations for a 10×10 site Hubbard system with $U = 8t$ at several average average densities and temperatures [23].

At high temperatures, of the order of $3t$, we find that density snapshots are fuzzy with no clear empty sites; mostly fluctuations about an average background density can be seen. This fuzziness is less of a concern for single-species snapshots (Fig. 1D), although they too lose their pixelated character at higher temperatures. For this reason, to eliminate fuzziness as an obvious feature for the CNN to learn, instead of high-temperature snapshots, we use low-temperature images whose pixels have been randomly shuffled, effectively destroying any physical correlations. In the following, we refer to the latter as *fake* (as opposed to *real*) snapshots.

Figure 2C shows sample filters from four different training experiments using theory snapshots of single species at $n = 0.82$. Despite reduced accuracies of about 68%, we find that the trained features are in excellent agreement with those obtained with quantum gas microscope snapshots. Results of other similar experiments [23] are all consistent with these findings and demonstrate that relevant spin correlations can be captured in an unbiased fashion through CNNs.

Studies of the origin of the NFL behavior, a central question in any theory of high-temperature superconduc-

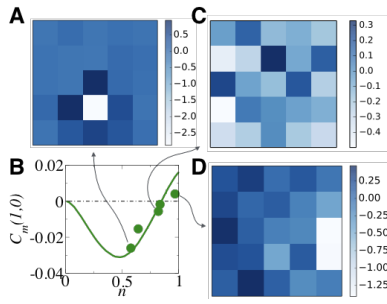


FIG. 3. **Analysis of local moment snapshots using CNNs with one filter.** Representative 5×5 filters for runs at (A) $n = 0.58$, (C) $n = 0.82$, and (D) $n = 0.97$ using the same CNN architecture as one used for snapshots of single species. (B) Shows the nearest-neighbor local moment correlation function from DQMC (solid line) on an 8×8 cluster at $T = 0.3t$ and from the experiment (circles) at similar low temperatures. The testing accuracy is 89% for A, 62% for C and 60% for D.

tivity [28], have for decades been focused on its possible connections to the order parameter fluctuations of a magnetic quantum critical point [28–34]. Here, we are in a position to ask whether any such fluctuations manifest themselves in charge correlations too, and to what extent they can be inferred from the other type of snapshots available in the experiment, those of local moments.

A similar analysis using images at the two extreme temperatures, however, is largely affected by the abundance of doubly occupied sites at $T \sim 7.5t$, and their lack of representation in the snapshots of local moments. Upon lowering the temperature to $T \sim 0.35t$, the fraction of doubly occupied sites at 18% doping reduces roughly by a factor of four from 12% to about 3%, providing the CNN again with an obvious feature with which to perform classification [23]. Removing this bias by randomly populating pixels to create “fake” replacements for high-temperature snapshots in the training, brings the accuracy down dramatically when $n = 0.82$.

Figure 3 shows that the accuracy of CNNs trained on snapshots of local moments largely depends on the strength of short-range correlations between the moments. The largest accuracies (almost 90%) are typically achieved near quarter filling, where the correlations are the most negative. Patterns observed in filters trained in this region are also consistent with the anti-correlation of neighboring moments (Fig. 3A). The accuracy drops to around 60% at $n = 0.82$, near the zero crossing of the correlator, which is shown in Fig. 3B. Typical trained filters do not display any immediately recognizable patterns either (Fig. 3C) [23]. Near half filling, the correlations between local moments are positive due to the bunching of holes and doubly occupied sites [35]. Here, we find that despite the relatively low accuracies ($\lesssim 65\%$), trained filters often do reflect the bunching of empty sites (Fig. 3D) [23].

The comparison of Fig. 3C ($n = 0.82$) with Figs. 3A and 3D ($n = 0.58, 0.97$) makes it clear that snapshots of local moments in the NFL region of the Hubbard model do not contain a single dominant ordering pattern and that a more advanced treatment may be necessary to capture the physics. In Fig. 4, we show results of a training with a CNN, modified to include six 7×7 filters in its convolutional layer [23]. The bigger dataset we have available for snapshots of local moments at this density allows us to experiment with different filter sizes and the number of filters. We find that including more than one filter in the CNN improves the best accuracies only marginally in this case, up to around 65%, and having too many and/or much larger filters can still result in overfitting.

Fig. 4A shows six filters of a sample CNN trained on the local moment snapshots. Their fuzzy patterns offer some insight into possible spatial arrangements of local moments at low temperatures. As we will see below, patterns in filters $m = 1, 4, 5$, and 6 are more frequently associated by the network with real low-temperature snapshots at this filling, whereas patterns in filter $m = 2$ are more frequently associated with fake snapshots.

It is worth noting that nonlinearities in the neural network model make the interpretation of features seen in the filters vis-à-vis correlations in the physical snapshots challenging since the knowledge of the network can be divided in nontrivial ways among its different components. An early example of this was the surprisingly successful classification of snapshots of the Ising lattice gauge theory at $T = 0$ and $T = \infty$, despite the lack of an order parameter, using CNNs with multiple filters [10].

By transferring the knowledge of the CNN to other densities, we find that the network is the most sensitive to correlations around the NFL region. Figure 4B shows the difference in probabilities that a snapshot and its fake counterpart are categorized as belonging to the NFL region; effectively eliminating density itself as a factor in the signal. We find this quantity to be maximal in the vicinity of $n = 0.8$, suggesting that the CNN as a whole is in fact focusing on local moment correlations more unique to the NFL region and slightly lower densities.

While the contribution of individual filters to the CNNs decision making cannot be completely isolated, we can study what the network output would be if each filter were to act alone [23]. Figure 4C shows this quantity averaged over samples at $n = 0.82$, after subtracting the value for the corresponding fake snapshot, for each of the six filters shown in Fig. 4A. The results suggest that filters 1 and 6, if acting alone, would have the largest effect on the decision making at this average density, followed by filters 2, 4 and 5, while filter 3 plays almost no role at all. The negative value for filter 2 indicates that the network signal is larger on average for fake snapshots in that case. A similar analysis of snapshots with information about both species of particles in future experi-

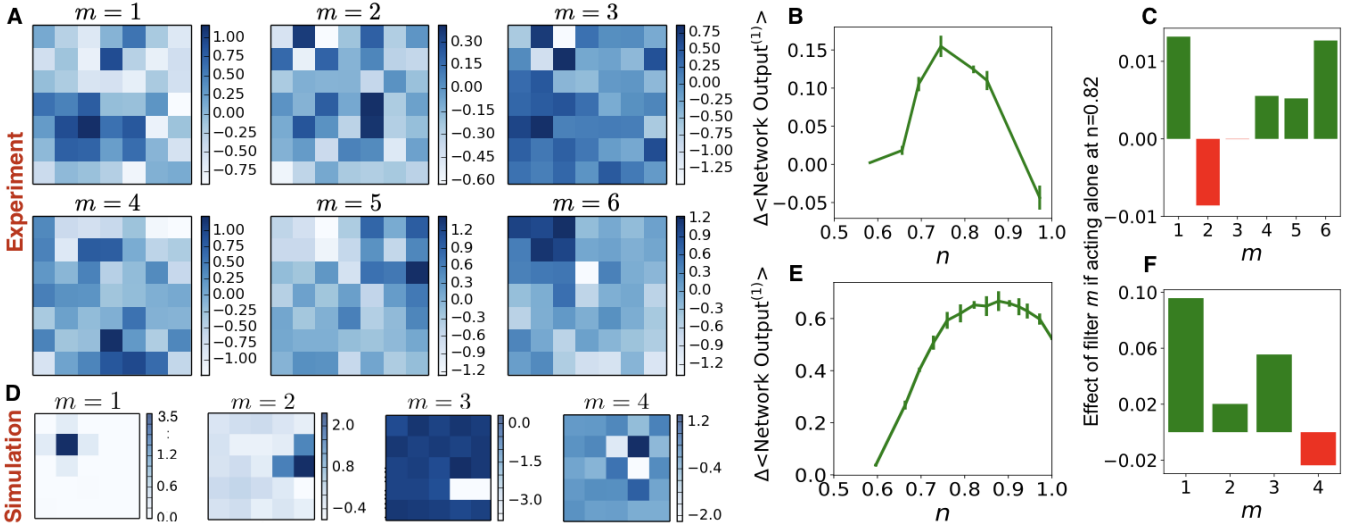


FIG. 4. **Analysis of local moment snapshots using CNNs with multiple filters.** (A) The six filters of a trained CNN. Training is performed with the 5023 experimental local moment snapshots taken at $n = 0.82$ and $T \sim 0.35$. The average testing accuracy in the last 20 epochs of the run is $62\% \pm 0.01\%$ [23]. (B) The difference in the average network output for $T \sim 0.35t$ real and fake snapshots as a function of the density when all six filters are present: $\Delta \langle \text{Network Output}^{(1)} \rangle \equiv \langle \text{Network Output}^{(1)}(\mathbf{X}^{\text{real}}) \rangle - \langle \text{Network Output}^{(1)}(\mathbf{X}^{\text{fake}}) \rangle$. Superscript (1) indicates the value at the output neuron responsible for real low-temperature snapshots [23]. This quantity indicates roughly the percentage of the output attributable to factors other than the density. (C) Similar to (B) at $n = 0.82$ when the CNN has access to one filter at a time. (D) Four representative filters of a CNN with sixteen 5×5 filters trained using DQMC snapshots of local moments [23]. (E) (F) Same as (B) (C), but obtained using the CNN in (D).

ments [36], may further reveal the interplay between spin and charge fluctuations in this region.

Using DQMC, we verify that similar trends can be observed in simulated snapshots of local moments. However, unlike with the experimental snapshots, here, we find that the accuracy generally increases with increasing the number of filters in the CNN, while increasing the filter size does not necessarily improve the performance. We attribute these to the fundamental difference between the two types of snapshots (projective vs non-projective). Figure 4D highlights a representative sample of 5×5 filters of a CNN with sixteen such filters, trained on simulated snapshots reaching to an accuracy of 87% [23]. They appear to measure a variety of short-range correlations to assist the network in making decisions. Figure 4E shows the overall signal of the CNN for correlations unique to the NFL phase, plotted across densities. It has a broad peak around the NFL region. As shown in Fig. 4F, patterns in the first three filters seem to be mostly associated with real snapshots in the NFL region, while the pattern in $m = 4$ filter is mostly associated with the fake snapshots. We find that including the information about doubly occupied sites, i.e., using full density snapshots, generally improves the diversity of features seen in the trained filters while yielding the same basic trends [23].

The techniques developed in this work for the AI-assisted feature extraction in projective measurements

can be adapted to peek into other mysterious phenomena for the Fermi-Hubbard model, such as the pseudogap phase [37], or the magnetic polaron which has been observed closer to half filling [38]. They can also be employed to study other microscopic models of correlated systems. Our work paves the way for AI related studies that go beyond mere categorization and the quest for gaining more predictive power and focus instead on the inner-workings of the machines to advance our understanding of complicated natural phenomena.

We thank Christie Chiu, Annabelle Bohrdt, and Neil Switz for useful discussions. E.K. acknowledges support from the National Science Foundation (NSF) under Grant No. DMR-1609560. Computations were performed in part on Spartan high-performance computing facility at San José State University, which is supported by the NSF under Grant No. OAC-16266. The work of R.T.S. was supported by the grant DESC0014671 funded by the U.S. Department of Energy, Office of Science. The work of E.G.-S., B.M.S. and W.S.B. was supported by the NSF under Grant No. DMR-1607277, the David and Lucile Packard Foundation under Grant No. 2016-65128, and the AFOSR Young Investigator Research Program under Grant No. FA9550-16-1-0269. J.C. acknowledges support from the Natural Sciences and Engineering Research Council of Canada (NSERC), the Shared Hierarchical Academic Research Computing Network (SHARCNET), Compute Canada, and the Canada CIFAR AI

chair program.

* ehsan.khatami@sjsu.edu

- [1] X. Wen, *Quantum Field Theory of Many-Body Systems: From the Origin of Sound to an Origin of Light and Electrons*, Oxford Graduate Texts (OUP Oxford, 2004).
- [2] J. Orenstein and A. J. Millis, *Science* **288**, 468 (2000).
- [3] C. Varma, Z. Nussinov, and W. van Saarloos, *Physics Reports* **361**, 267 (2002).
- [4] S. Sachdev and D. Chowdhury, *Progress of Theoretical & Experimental Ph* **2016** (2016), 10.1093/ptep/ptw110.
- [5] Y. Cao, V. Fatemi, S. Fang, K. Watanabe, T. Taniguchi, E. Kaxiras, and P. Jarillo-Herrero, *Nature* **556**, 43 (2018).
- [6] Y. Cao, V. Fatemi, A. Demir, S. Fang, S. L. Tomarken, J. Y. Luo, J. D. Sanchez-Yamagishi, K. Watanabe, T. Taniguchi, E. Kaxiras, R. C. Ashoori, and P. Jarillo-Herrero, *Nature* **556**, 80 (2018).
- [7] P. T. Brown, D. Mitra, E. Guardado-Sanchez, P. Schauß, S. S. Kondov, E. Khatami, T. Paiva, N. Trivedi, D. A. Huse, and W. S. Bakr, *Science* **357**, 1385 (2017).
- [8] P. T. Brown, D. Mitra, E. Guardado-Sanchez, R. Nourafkan, A. Reymbaut, C.-D. Hébert, S. Bergeron, A.-M. S. Tremblay, J. Kokalj, D. A. Huse, P. Schauß, and W. S. Bakr, *Science* **363**, 379 (2019).
- [9] G. Carleo and M. Troyer, *Science* **355**, 602 (2017).
- [10] J. Carrasquilla and R. G. Melko, *Nat. Phys.* **13**, 431 (2017).
- [11] K. Ch'ng, J. Carrasquilla, R. G. Melko, and E. Khatami, *Phys. Rev. X* **7**, 031038 (2017).
- [12] D.-L. Deng, X. Li, and S. Das Sarma, *Phys. Rev. B* **96**, 195145 (2017).
- [13] E. P. L. van Nieuwenburg, Y.-H. Liu, and S. D. Huber, *Nat. Phys.* **13**, 435 (2017), letter.
- [14] Y. Zhang and E.-A. Kim, *Phys. Rev. Lett.* **118**, 216401 (2017).
- [15] Y. Zhang, A. Mesaros, K. Fujita, S. D. Edkins, M. H. Hamidian, K. Ch'ng, H. Eisaki, S. Uchida, J. C. S. Davis, E. Khatami, and E.-A. Kim, *Nature* **570**, 484 (2019).
- [16] A. Bohrdt, C. S. Chiu, G. Ji, M. Xu, D. Greif, M. Greiner, E. Demler, F. Grusdt, and M. Knap, *Nature Physics* **15**, 921 (2019).
- [17] B. S. Rem, N. Käming, M. Tarnowski, L. Asteria, N. Fläschner, C. Becker, K. Sengstock, and C. Weitenberg, *Nature Physics* **15**, 917 (2019).
- [18] G. Torlai, B. Timar, E. P. L. van Nieuwenburg, H. Levine, A. Omran, A. Keesling, H. Bernien, M. Greiner, V. Vuletić, M. D. Lukin, R. G. Melko, and M. Endres, *Phys. Rev. Lett.* **123**, 230504 (2019).
- [19] A. M. Samarakoon, K. Barros, Y. W. Li, M. Eisenbach, Q. Zhang, F. Ye, V. Sharma, Z. L. Dun, H. Zhou, S. A. Grigera, C. D. Batista, and D. A. Tennant, *Nature Communications* **11**, 892 (2020).
- [20] P. B. Wigley, P. J. Everitt, A. van den Hengel, J. W. Bastian, M. A. Sooriyabandara, G. D. McDonald, K. S. Hardman, C. D. Quinlivan, P. Manju, C. C. N. Kuhn, I. R. Petersen, A. N. Luiten, J. J. Hope, N. P. Robins, and M. R. Hush, *Scientific Reports* **6**, 25890 EP (2016).
- [21] L. R. B. Picard, M. J. Mark, F. Ferlino, and R. van Bijnen, *Measurement Science and Technology* **31**, 025201 (2019).
- [22] M. D. Zeiler and R. Fergus, “Visualizing and understanding convolutional networks,” in *Computer Vision – ECCV 2014*, edited by D. Fleet, T. Pajdla, B. Schiele, and T. Tuytelaars (Springer International Publishing, Cham, 2014) pp. 818–833.
- [23] Materials and methods are available as supplementary materials.
- [24] J. Tranquada, “Neutron scattering studies of antiferromagnetic correlations in cuprates,” in *Handbook of High-Temperature Superconductivity*, edited by S. J.R. and B. J.S. (Springer, New York, NY, 2007).
- [25] R. Blankenbecler, D. J. Scalapino, and R. L. Sugar, *Phys. Rev. D* **24**, 2278 (1981).
- [26] M. Rigol, T. Bryant, and R. R. P. Singh, *Phys. Rev. Lett.* **97**, 187202 (2006).
- [27] E. Khatami and M. Rigol, *Phys. Rev. A* **84**, 053611 (2011).
- [28] S. Sachdev, *Physica Status Solidi (b)* **247**, 537 (2010).
- [29] J. A. Hertz, *Phys. Rev. B* **14**, 1165 (1976).
- [30] S. Sachdev and J. Ye, *Phys. Rev. Lett.* **69**, 2411 (1992).
- [31] A. J. Millis, *Phys. Rev. B* **48**, 7183 (1993).
- [32] G. R. Stewart, *Rev. Mod. Phys.* **73**, 797 (2001).
- [33] H. v. Löhneysen, A. Rosch, M. Vojta, and P. Wölfle, *Rev. Mod. Phys.* **79**, 1015 (2007).
- [34] A. L. Fitzpatrick, S. Kachru, J. Kaplan, and S. Raghu, *Phys. Rev. B* **88**, 125116 (2013).
- [35] L. W. Cheuk, M. A. Nichols, K. R. Lawrence, M. Okan, H. Zhang, E. Khatami, N. Trivedi, T. Paiva, M. Rigol, and M. W. Zwierlein, *Science* **353**, 1260 (2016).
- [36] J. Koepsell, S. Hirthe, D. Bourgund, P. Sompet, J. Vijayan, G. Salomon, C. Gross, and I. Bloch, *arXiv:2002.07577 [cond-mat.quant-gas]*.
- [37] C. S. Chiu, G. Ji, A. Bohrdt, M. Xu, M. Knap, E. Demler, F. Grusdt, M. Greiner, and D. Greif, *Science* **365**, 251 (2019).
- [38] J. Koepsell, J. Vijayan, P. Sompet, F. Grusdt, T. A. Hilker, E. Demler, G. Salomon, I. Bloch, and C. Gross, *Nature* **572**, 358 (2019).
- [39] S. R. White, D. J. Scalapino, R. L. Sugar, E. Y. Loh, J. E. Gubernatis, and R. T. Scalettar, *Phys. Rev. B* **40**, 506 (1989).
- [40] F. Assaad and H. Evertz, “World-line and determinantal quantum monte carlo methods for spins, phonons and electrons,” in *Computational Many-Particle Physics*, edited by H. Fehske, R. Schneider, and A. Weiße (Springer Berlin Heidelberg, Berlin, Heidelberg, 2008) pp. 277–356.
- [41] I. Jolliffe, *Principal component analysis* (John Wiley and Sons, Ltd, 2002).
- [42] L. Maaten and G. Hinton, *Journal of Machine Learning Research* **9**, 2579 (2008).
- [43] A tutorial on how to use t-SNE effectively can be found at <https://distill.pub/2016/misread-tsne>.
- [44] L. Wang, *Phys. Rev. B* **94**, 195105 (2016).
- [45] Codes available at <https://lvdmaaten.github.io/tsne> (2017).
- [46] M. Abadi, *et al.*, TensorFlow: Large-scale machine learning on heterogeneous systems (2015). Software available from tensorflow.org.
- [47] E. Y. Loh, J. E. Gubernatis, R. T. Scalettar, S. R. White, D. J. Scalapino, and R. L. Sugar, *Phys. Rev. B* **41**, 9301 (1990).
- [48] M. Troyer and U.-J. Wiese, *Phys. Rev. Lett.* **94**, 170201 (2005).

(2005).

[49] V. I. Iglovikov, E. Khatami, and R. T. Scalettar, Phys. Rev. B **92**, 045110 (2015).

Supplemental Information: Visualizing Correlations in the 2D Fermi-Hubbard Model with AI

Ehsan Khatami,¹ Elmer Guardado-Sanchez,² Benjamin M. Spar,²
Juan Felipe Carrasquilla,³ Waseem S. Bakr,² and Richard T. Scalettar⁴

¹*Department of Physics and Astronomy, San José State University, San José, CA 95192, USA*

²*Department of Physics, Princeton University, Princeton, NJ 08544, USA*

³*Vector Institute, MaRS Centre, Toronto, Ontario, M5G 1M1, Canada*

⁴*Department of Physics, University of California, Davis, CA 95616, USA*

THE MODEL

The Hamiltonian for the 2D Fermi-Hubbard model in particle-hole symmetric form is expressed as

$$\hat{H} = -t \sum_{\langle \mathbf{i}, \mathbf{j} \rangle} \left(\hat{c}_{\mathbf{i}}^{\dagger} \hat{c}_{\mathbf{j}} + \text{H.c.} \right) + U \sum_{\mathbf{i}} \left(\hat{n}_{\mathbf{i}\uparrow} - \frac{1}{2} \right) \left(\hat{n}_{\mathbf{i}\downarrow} - \frac{1}{2} \right) - \mu \sum_{\mathbf{i}} (\hat{n}_{\mathbf{i}\uparrow} + \hat{n}_{\mathbf{i}\downarrow}), \quad (1)$$

where $\hat{c}_{\mathbf{i}\sigma}^{\dagger}$ ($\hat{c}_{\mathbf{i}\sigma}$) creates (annihilates) a fermion with spin σ on site \mathbf{i} , and $\hat{n}_{\mathbf{i}\sigma} = \hat{c}_{\mathbf{i}\sigma}^{\dagger} \hat{c}_{\mathbf{i}\sigma}$ is the number operator. $\langle \dots \rangle$ denotes nearest neighbors on a square lattice, $U = 8t$ is the strength of the onsite repulsive interaction in the numerical simulations, and μ is the chemical potential. $\mu = 0$ corresponds to half filling, although density fluctuations around half filling exist in our grand canonical ensemble. $t = 1$ (also $\hbar = 1$ and $k_B = 1$) sets the energy scale. The spin correlation function is calculated as $C_s(\mathbf{r}) = \langle \hat{S}_{z,\mathbf{i}} \hat{S}_{z,\mathbf{i}+\mathbf{r}} \rangle$, where $\hat{S}_{z,\mathbf{i}} = \frac{1}{2}(\hat{n}_{\mathbf{i}\uparrow} - \hat{n}_{\mathbf{i}\downarrow})$. The local moment moment correlation function is calculated as $C_m(\mathbf{r}) = \langle \hat{m}_{z,\mathbf{i}}^2 \hat{m}_{z,\mathbf{i}+\mathbf{r}}^2 \rangle$, where $\hat{m}_{z,\mathbf{i}}^2 = (\hat{n}_{\mathbf{i}\uparrow} - \hat{n}_{\mathbf{i}\downarrow})^2$.

NUMBER OF AVAILABLE EXPERIMENTAL SNAPSHOTS AT $T \sim 0.35$

	$n = 0.97$	$n = 0.835$	$n = 0.82$	$n = 0.735$	$n = 0.70$	$n = 0.64$	$n = 0.58$
Spin-up/Spin-down	402	-	302	-	-	-	-
Singles	201	281	5023	290	342	281	330

TABLE I. Number of available experimental snapshots at $T \sim 0.35$ for different densities.

DETERMINANTAL QUANTUM MONTE CARLO AND THEORY SNAPSHOTS

The implementation of determinantal Quantum Monte Carlo (DQMC) used in the work proceeds via the exact rewriting of the interacting electron-electron problem as independent electrons moving in a space-imaginary time

auxiliary field $h(\mathbf{r}, \tau)$. This reformulation involves first expressing the partition function \mathcal{Z} for the original Hubbard Hamiltonian as a path integral, and then the use of a Hubbard-Stratonovich transformation to decouple the electrons. The original fermionic degrees of freedom are then traced out analytically, leaving an equivalent expression for \mathcal{Z} as an integral over $h(\mathbf{r}, \tau)$. Detailed descriptions can be found in [25, 39, 40].

Here we focus on aspects of DQMC which have specific implications to the machine learning process. The most crucial is that, unlike world-line QMC methods or cold-atom experiments, which directly sample the 0 or 1 occupation of sites \mathbf{r} by the fermions, at any point (snapshot) in a DQMC simulation, the fermionic occupation is represented by a real number giving the probability of occupation of that site in the specific $h(\mathbf{r}, \tau)$ currently being sampled. As the temperature is lowered below t , sharper images containing pixels more closely resembling binary pixels in the experimental snapshots emerge. In fact, one can show that in the atomic limit, local expectation values approach step functions as $T \rightarrow 0$. This ‘smearing’ of the occupation makes some aspects of machine learning via these snapshots more challenging. However, whether individual snapshots present (0,1) fermion occupations or not, the strong correlation physics (magnetism, superconductivity, strange metallicity) of the Hubbard model needs to be built up from many thousands of snapshots. It is the task of uncovering these many-body effects that is shared by the theoretical and experimental images investigated here with AI.

We have also generated projective measurements on small 8- and 10-site periodic clusters using exact diagonalization and sampling at finite temperatures. However, the significant boundary effects render any comparison of training results at finite doping to experiments useless.

FOURIER ANALYSIS OF THE SNAPSHOTS

Figure 5 shows averages of the magnitude of Fourier coefficients of several different sets of snapshots at low temperatures. We find that, other than those corresponding to the expected $\mathbf{k} = \mathbf{0}$ or \mathbf{k} in the vicinity of (π, π) (for the single-species snapshots), there do not exist any other significant arrangements of fermions on the lattice captured through the linear Fourier transformation.

Figure 6 shows the percentage of weight associated with \mathbf{k} points other than $\mathbf{k} = \mathbf{0}$ in the Fourier transform of the average snapshot. The suppression of this quantity as the number of snapshots increases makes clear that fluctuations inferred through Fourier transform are expected to decrease on average. They vanish for theory in the limit of infinite number of snapshots. However, inhomogeneities in the trapping potential can prevent that from happening for the

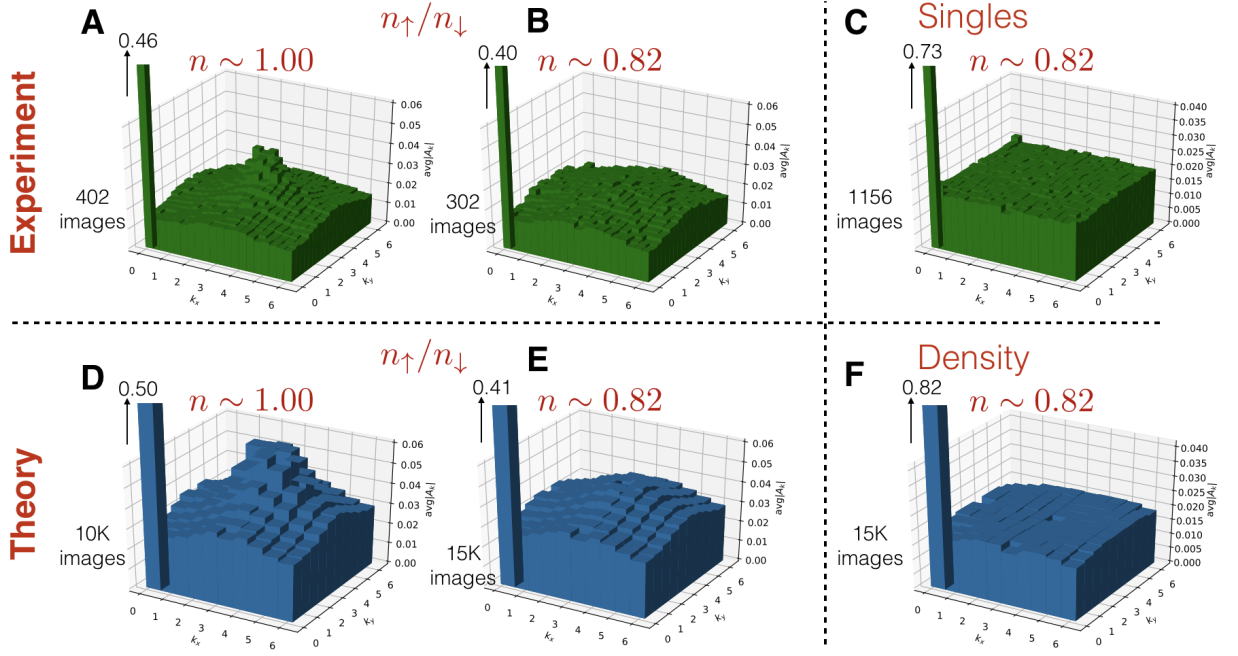


FIG. 5. **Averages of the magnitude of Fourier coefficients of snapshots in different cases.** (A), (B) and (C) show results for experimental snapshots of single-species fermions for $n \sim 1$ and $n = 0.82$ and snapshots of local moments (singles) for $n = 0.82$, respectively, all at $T \sim 0.35t$. (D), (E) and (F) show results for the theory snapshots at $T = 0.44t$.

experimental snapshots, even in the limit of infinite number of snapshots. As discussed below, we mitigate the issue when the CNN is sensitive to the inhomogeneities by creating fake snapshots that have the same average pixel values as the corresponding real ones.

UNSUPERVISED LEARNING

We have employed two unsupervised learning algorithms, the linear principal component analysis (PCA) [41] and the nonlinear t-distributed stochastic neighbor embedding (tSNE) [42, 43], to perform dimensional reduction on the experimental snapshots of single species at $n = 0.82$. In doing so, features may emerge in the low-dimensional space revealing certain repeated patterns in the snapshots.

In the PCA, one forms a *matrix of data*, \mathbf{x} by flattening the matrix of pixel values for each snapshot and placing them as an array of 400 binary numbers in each row (of \mathbf{x}). In the next step, the covariance matrix of data is composed as $\mathbf{x}^T \cdot \mathbf{x}$. Diagonalizing the 400×400 matrix, we obtain its eigenvalues, whose magnitudes are a measure for the variance of the data along the *principal axes*, determined by the corresponding eigenvectors. As demonstrated for the two-dimensional Ising model in a pioneering application in physics [44], a dominant eigenvalue is indicative of a clear distinguishing pattern in the snapshots that can be represented as a linear combination of its pixels (their projection

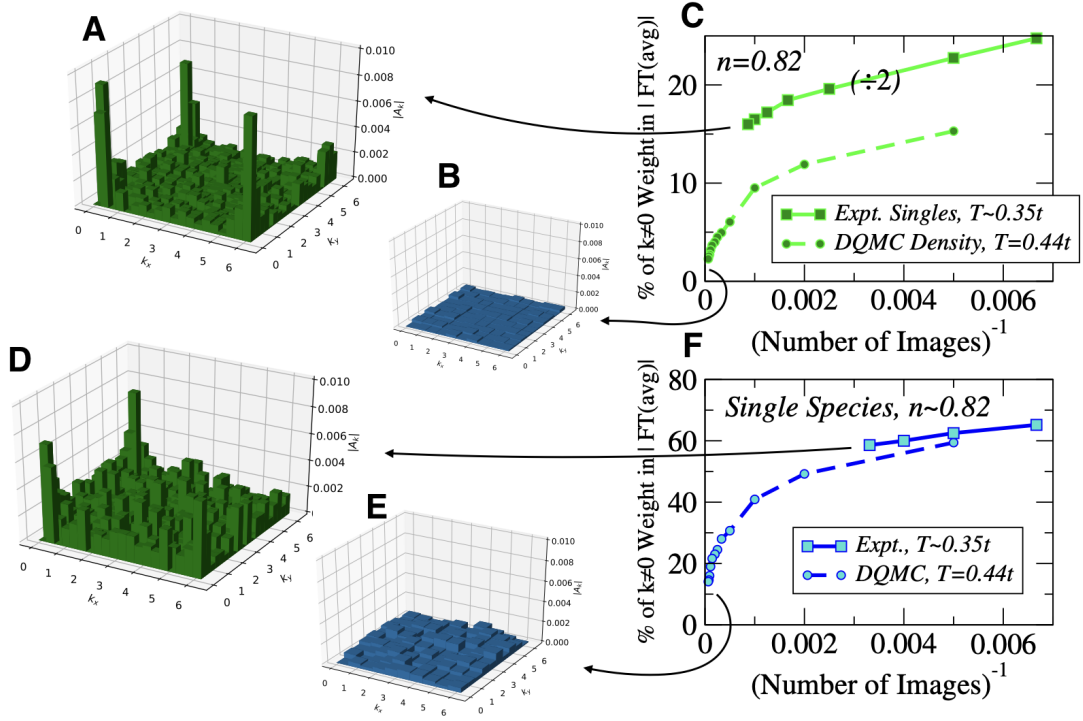


FIG. 6. **Percentage of $k \neq 0$ weight in the magnitude of the Fourier transform of the average snapshot.** Increasing the number of snapshots leads to the suppression of this quantity, showing that on average, there are no inhomogeneities in the data.

to the corresponding principal axis).

tSNE on the other hand, is a nonlinear method that minimizes the Kullback-Leibler divergences between pairwise conditional probability distributions, representing similarity of points, from the high- and low-dimensional spaces (for a more detailed discussion see Ref. [42]). Here, we have used the implementation in Ref. [45].

Figure 7 shows our results in the two-dimensional space from both algorithms. Neither method seems to be

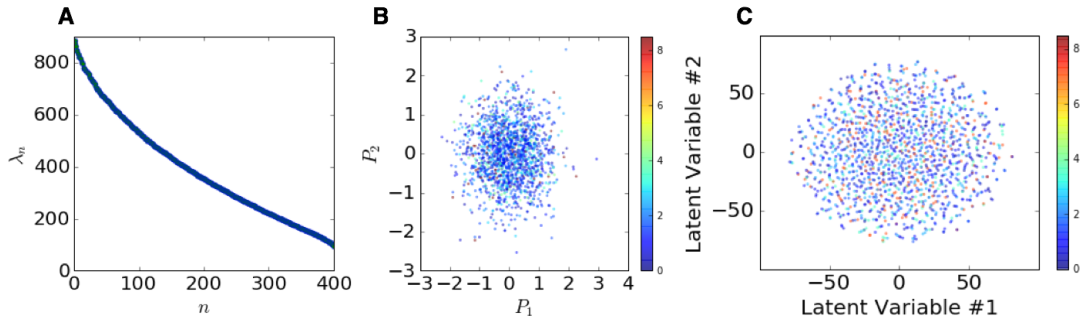


FIG. 7. **The application of the PCA and the tSNE algorithms to the experimental snapshots of single species at $n = 0.82$ across a range of temperatures.** (A) The eigenvalues of the covariance matrix of data showing no outstanding principal components. (B) The projection of data to the two-dimensional space of the two largest principal components. The color bar denotes the temperature. Many of the high-temperature points overlap with their lower-temperature counterparts. No discernible patterns emerge in this projection. (C) Projection of data to the space of non-linear latent variables obtained in the tSNE analysis. A “perplexity” of 30 has been used here. No discernible patterns emerge.

able to draw any particular distinction between low and high temperature snapshots as there are no signs of any clustering of data points based on temperature. Figure 7A shows the eigenvalues of the covariance matrix of data and further proves that there is no linear combination of pixel values that could serve as a clear indicator for differences between snapshots at different temperatures. In Fig. 7B, we have projected the data into the space of the two linear combinations (principal axes) corresponding to the largest two eigenvalues. They represent the directions of the largest variance in data. As expected from Fig. 7A, all the points belong to one single symmetric cluster with no discernible features.

Likewise, Fig. 7C shows the same data projected into the space of tSNE’s two latent variables and does not display formation of any particular features. Changing the “perplexity” variable in the algorithm, the number of iterations, or the number of principal components kept from an initial PCA reduction before tSNE is applied does not significantly change this result.

TRAINING THE CONVOLUTIONAL NEURAL NETWORK

We implement our CNNs using Tensorflow [46]. The minimalistic design in Fig. 1C we have adopted reflects the need to reduce the number of free parameters to avoid overfitting given the sizes of our data sets. To train, we assign a label, Y to each snapshot based on the temperature at which it is taken, or whether it is real or fake. Each label is stored in the one-hot format, i.e., a binary array of two numbers, one of which is 1 and the other 0. The index for 1 indicates the category (high/low temperature, or real/fake) to which each snapshot belongs. Given an input image \mathbf{X} , the value arriving at the first of the two output neurons of the CNN shown in Fig. 1C, e.g., at the neuron we have associated in our labels to the low-temperature (or real) snapshots, is

$$O_1^{out}(\mathbf{X}) = \sum_h O_h^{hid}(\mathbf{X}) \times W_h^{out(1)} + b^{out(1)}, \quad (2)$$

where the sum is over hidden neurons,

$$O_h^{hid}(\mathbf{X}) = \text{ReLU} \left(\left[\frac{1}{N_s} \sum_{stride:s} \text{ReLU}(\mathbf{W}^{filter} \cdot \mathbf{X}(s) + b^{filter}) \right] \times W_h^{hid} + b_h^{hid} \right), \quad (3)$$

N_s is the number of strides the filter takes around the image convolving with different sections of it, \mathbf{W}^{filter} is the matrix of pixel values for the filter, $\mathbf{X}(s)$ is the matrix of pixel values for the section of the image the filter is convolving

with in stride s , ReLU is the rectified linear unit activation function, and b^{filter} , W_h^{hid} , b_h^{hid} , $W_h^{out(1)}$ and $b^{out(1)}$, are numbers representing other weights and biases in the network. O_1^{out} , along with the value arriving at the second output layer $O_2^{out}(\mathbf{X})$ are then passed through the softmax activation function in order to obtain two probabilities as network outputs:

$$[\text{Network Output}^{(1)}(\mathbf{X}), \text{Network Output}^{(2)}(\mathbf{X})] = \text{softmax}[O_1^{out}(\mathbf{X}), O_2^{out}(\mathbf{X})]. \quad (4)$$

The input snapshot is classified as belonging to category i if O_i^{net} is the higher probability. The accuracy is defined as the percentage of correct classifications given known labels Y . The convolution of the trained filter with sections of the input image as it moves around in strides of one in every direction creates a “feature map” in which large overlaps between patterns in the filter and the image are highlighted.

For training, we use the Adam optimizer, which is an extension of stochastic gradient descent, to minimize the cross-entropy cost function, defined as

$$c = -\frac{1}{N_d} \sum_{\mathbf{X}} \sum_{i=1}^2 (Y_i(\mathbf{X}) \ln[O_i^{net}(\mathbf{X})] + [1 - Y_i(\mathbf{X})] \ln[1 - O_i^{net}(\mathbf{X})]), \quad (5)$$

where $O_i^{net} = \text{Network Output}^{(i)}$ for brevity, N_d is the number of data. During the training, we keep between 10% and 20% of the snapshots from the CNN and use them to perform unbiased testing of the accuracy.

CNN with More than One Filter

In cases where we have more than one filter in the convolutional layer, we have modified the architecture to have no fully connected hidden layer in order to reduce the total number of network parameters; the output of each filter after pooling is instead fully connected to the output layer. The value arriving at the output neuron that is responsible for firing when a real snapshot \mathbf{X} is provided to the input, $O_1^{out}(\mathbf{X})$, can then be expressed as a linear combination of contributions from individual filters:

$$O_1^{out}(\mathbf{X}) = \sum_{m=1}^{N_f} F_m^{(1)}(\mathbf{X}) \quad (6)$$

$$F_m^{(1)}(\mathbf{X}) = \left[\frac{1}{N_s} \sum_{stride:s} \text{ReLU}(\mathbf{W}_m^{filter} \cdot \mathbf{X}(s) + b_m^{filter}) \times W_m^{out(1)} \right] + \frac{b^{out(1)}}{N_f}, \quad (7)$$

where N_f is the number of filters, and $W_m^{out(1)}$ and b_m^{filter} are again numbers representing other weights and biases in the network. As in the case of the CNN with one filter, the network output is obtained using Eq. 4.

Effect of Individual Filters

To estimate the effect of filter m on the outcome, we replace $O^{(1,2)}(\mathbf{X})$ with $F_m^{(1,2)}(\mathbf{X})$ before the softmax function,

$$[\text{Network Output}_m^{(1)}(\mathbf{X}), \text{Network Output}_m^{(2)}(\mathbf{X})] = \text{softmax}[F_m^{(1)}(\mathbf{X}), F_m^{(2)}(\mathbf{X})], \quad (8)$$

so that we can interpret $\left[\text{Network Output}_m^{(1)}(\mathbf{X}^{real}) - \text{Network Output}_m^{(1)}(\mathbf{X}^{fake}) \right]$ as the percentage the network output for \mathbf{X} , based on the action of filter m alone, has to do with factors other than the density itself.

TRAINING PROGRESSION

To monitor the training progression and look for signs of overfitting, especially in the case of CNNs with more than one filter, we track the training and the unbiased testing accuracies over *epochs*. An epoch is when the network has gone over the entire dataset once. In Fig. 8A, we show these quantities for the case of training with experimental snapshots of local moment leading to the results in Fig. 4. Despite the deviation of the average of two accuracies from each other beyond $\sim 1,000$ epochs, signaling the beginning of overfitting due to the relatively large number of free parameters in the CNN, large fluctuations in the accuracies cause occasional overlapping of the two curves even after 5,000 epochs.

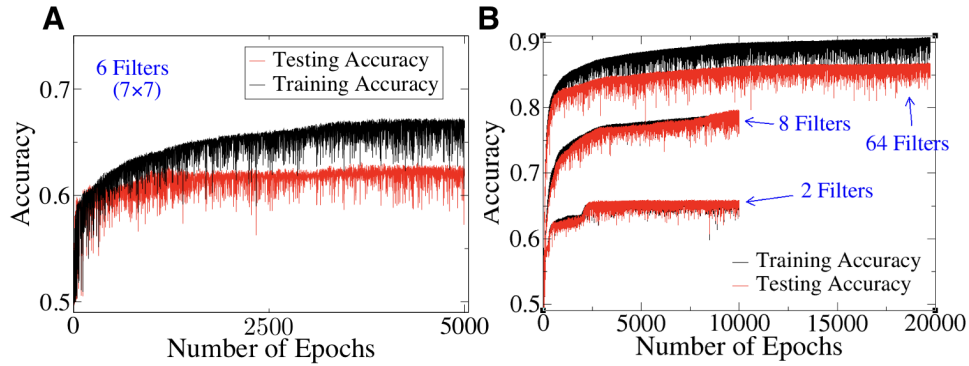


FIG. 8. **Progression of CNN's accuracy during training for several different cases.** (A) For the training with experimental snapshots of local moments using a CNN with six 7×7 filters (Fig. 4). (B) For trainings with DQMC density snapshots using CNNs with 2, 8 and 64 5×5 filters.

Figure 8B shows a similar training progression for CNNs used for DQMC snapshots of density with various numbers of filters. One can see signs of overfitting when the number of filters is increased to 64.

ALTERNATIVE TRAININGS WITH SNAPSHOTS OF SINGLE SPECIES

Figure 9 displays results of a training with single-species experimental snapshots at $n = 0.82$, however, using a strategy similar to that adopted for the DQMC snapshots in Fig. 2C; using low-temperature snapshots with randomly shuffled pixels (fake snapshots) in place of those at the highest temperature in the training. We find that similar nearest-neighbor anti-correlation features observed in both Fig. 2A and C emerge in the trained filters in this case.

One may wonder what happens if we trained not on data with the most extreme temperature difference, but those from closer temperatures. Figure 10 shows the results for training using experimental snapshots at $T \sim t$ and $T \sim 0.35t$. Some of the same features as in Fig. 2 are visible in these panels. However, they appear messier and less refined. The accuracies also drop to around 70%, which are consistent with the limiting case expectation; that telling apart snapshots at the same temperature, only labeled differently, must be only 50% effective.

Changing the filter size does not significantly affect our findings. Figure 11 shows a sample of four 3×3 filters trained on the same data as for Fig. 2A also yielding testing accuracies of at least 86%. The features obtained very much resemble those seen in Fig. 2A, albeit through a smaller lens; they too mostly point to nearest-neighbor anti-correlations between particles.

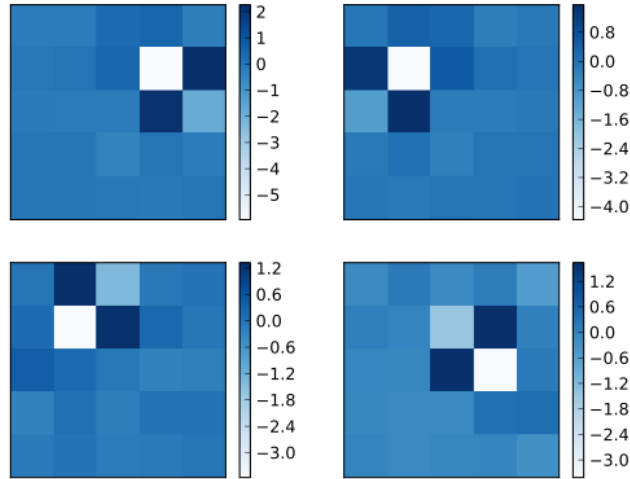


FIG. 9. **Training runs using real and fake experimental snapshots for $n = 0.82$.** Same as Fig. 2A, except that instead of experimental snapshots at $T \sim 7.5t$ images generated by randomly shuffling pixels of low-temperature snapshots are used. The testing accuracy is at least 93%.

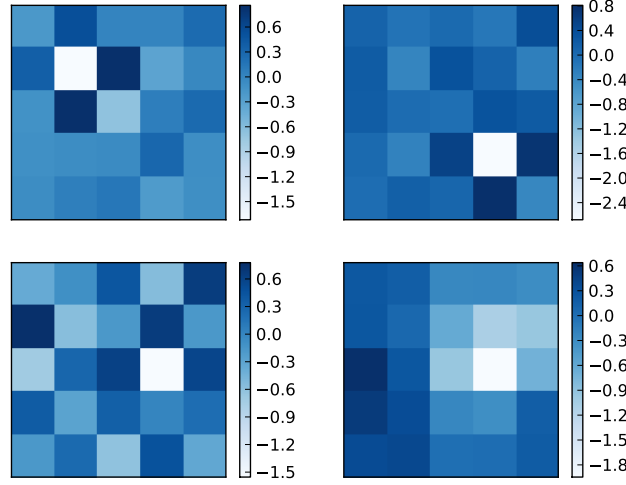


FIG. 10. **Training runs using experimental snapshots for $n = 0.82$ at close temperatures.** Similar to Fig. 2A, except that the training has been done to distinguish snapshots at $T \sim t$ from those $T \sim 0.35t$. The testing accuracies are around 70%.

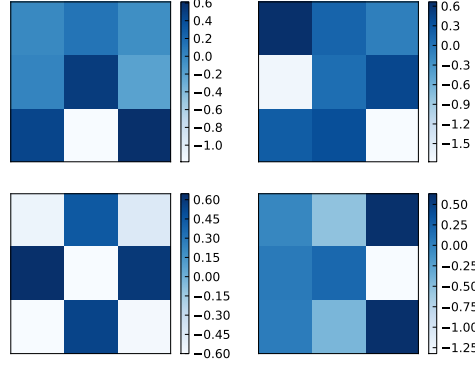


FIG. 11. **Training runs using smaller filters.** Similar to Fig. 2A, except that the training has been done using 3×3 filters. The testing accuracies are at least 86%.

With DQMC, we also have access to *spin* snapshots, as they can be obtained by subtracting snapshots of spin-up and spin-down density for the same instance of the auxiliary field. Figure 12 shows that training with those images yields the same features in filters as seen in training with spin-up or spin-down snapshots.

No discernible features emerge in the filters trained on the snapshots of local moments (experimental singles) at the two extreme temperatures (see Fig. 13A) despite near perfect accuracies ($> 95\%$) found for the CNN in predicting to which temperature each snapshot belongs. To reconcile the seemingly random patterns developing in the filters with the incredibly high predicting accuracies they provide for the CNN, we have examined the resulting feature maps and found that in every case, the network bases its decision essentially on the number of empty sites in every snapshot. This is a convenient feature for the network as there is a significantly larger number of them at the higher temperature due to the larger fraction of the doubly occupied sites (Fig. 13B), and the fact that they show up as fermion holes in

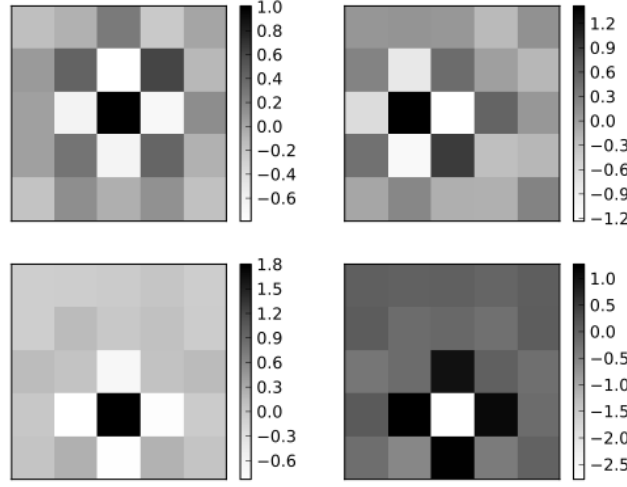


FIG. 12. **Training runs using DQMC snapshots of spin.** Same as Fig. 2C, except that DQMC snapshots of spin have been used in the training.

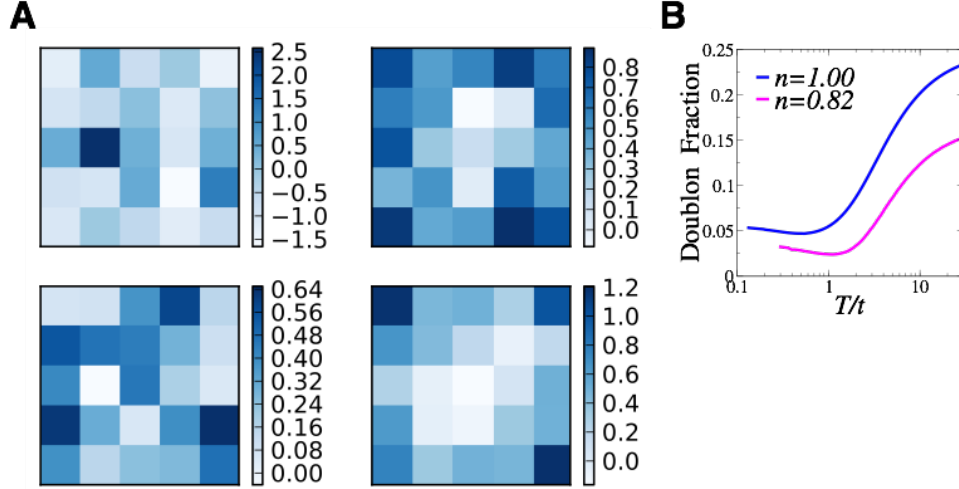


FIG. 13. **Training runs using experimental snapshots of local moment at the extreme temperatures.** (A) Same as in Fig. 2A, except that experimental snapshots of local moments are used in the training. The testing accuracies here are at least 95%. (B) Fraction of doubly occupied sites of the Fermi-Hubbard model in the thermodynamic limit as a function of temperature for $U = 8t$ at half filling and $n = 0.82$ from a numerical linked-cluster expansion. It decreases by about 70% when at $n = 0.82$, temperature decreases from $\sim 7.5t$ to $\sim 0.35t$.

the snapshots of local moments.

This is also supported by our observation that artificially increasing the value of pixels at occupied sites of high-temperature snapshots to match their average density of fermions with those in the low-temperature snapshots does not hinder the CNN's predictive ability. On the other hand, using fake snapshots in place of high-temperature ones and keeping the average density at every pixel the same as for low-temperature snapshots to also account for the slight inhomogeneities in the trapping potential, leads to a sharp drop in the predicting accuracy to about 60%.

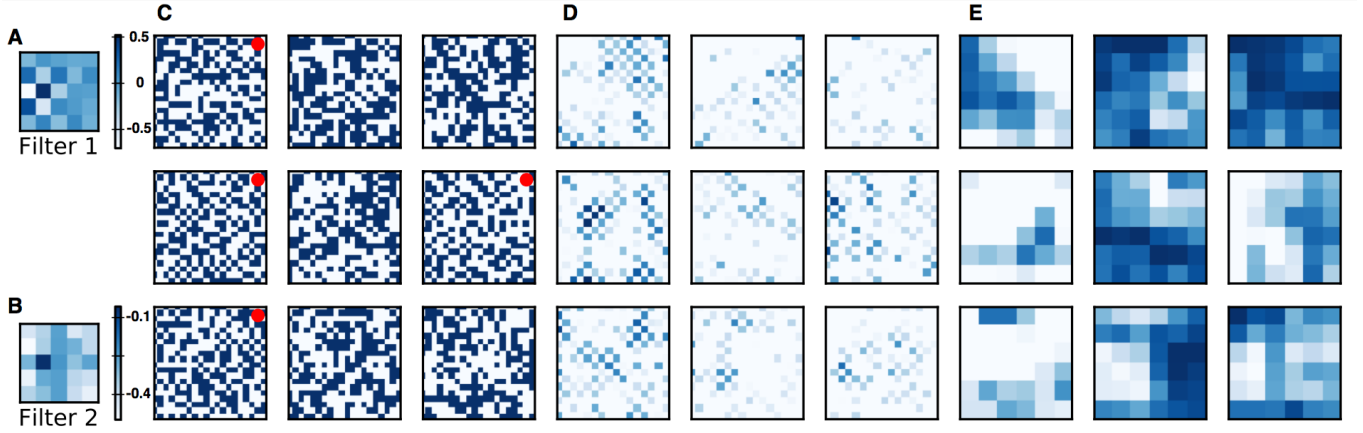


FIG. 14. **Output of a CNN with two convolutional layers trained on experimental snapshots of single species for $n \sim 1.0$.** (A) and (B) Trained filters in the first and second convolutional layers immediately after the input layer, respectively. (C) Nine sample inputs of single-species snapshots at the two extreme temperatures of $T \sim 0.35t$ (marked by a red dot at the corner of the image) and $T \sim 2.5t$. (D) Corresponding feature maps from the first convolutional layer. Stride of one in each direction has been used. The color bars are the same as in (A) with the maximum/minimum fixed at 0.0/1.5. (E) Corresponding feature maps from the second convolutional layer. Stride of one in each direction has been used. No pooling has been used between the two convolutional layers. The color bars are the same as in (A) with the maximum/minimum fixed at 0.0/1.4. After being trained, the network constructs features maps in the second layer that have a lower density for low-temperature snapshots as a way to facilitate decision making.

A DEEPER NETWORK FOR HALF FILLING

Since we have access to more single-species snapshots at half filling than at $n \sim 0.82$, we have also tried training a CNN with two consecutive convolutional layers after the input layer, each with one 5×5 filter. The trained filters and the output of each of the convolutional layers (feature maps) for nine sample input snapshots are shown in Fig. 14. Four of the sample snapshots, denoted by a red circle at their top right corner, belong to the low-temperature set with significant AF ordering present, and the other five are high-temperature snapshots. The first filter, directly in contact with the input, clearly picks up AF correlations as the feature to look for (Fig. 14A), similar to those shown in Fig. 2B for a CNN with a single convolutional layer. Therefore, the resulting feature maps, shown in Fig. 14D, reflect the same correlations, which appear stronger and more widespread for the low-temperature snapshots.

Here, the second convolutional layer operates directly on feature maps obtained by the filter in the first layer. The trained filter in the second layer is shown in Fig. 14B. The pixels with relatively small negative values seen in this filter, along with the ReLU activation function, help the network identify the empty regions in the feature maps with which the filter convolves. This can be seen in the resulting feature maps of the second convolutional layer (Fig. 14E). Regions with significant checkerboard patterns in the first set of feature maps translate to mostly empty regions in the second set of feature maps. Pooling the pixel values in the latter results in a number that is smaller/larger than

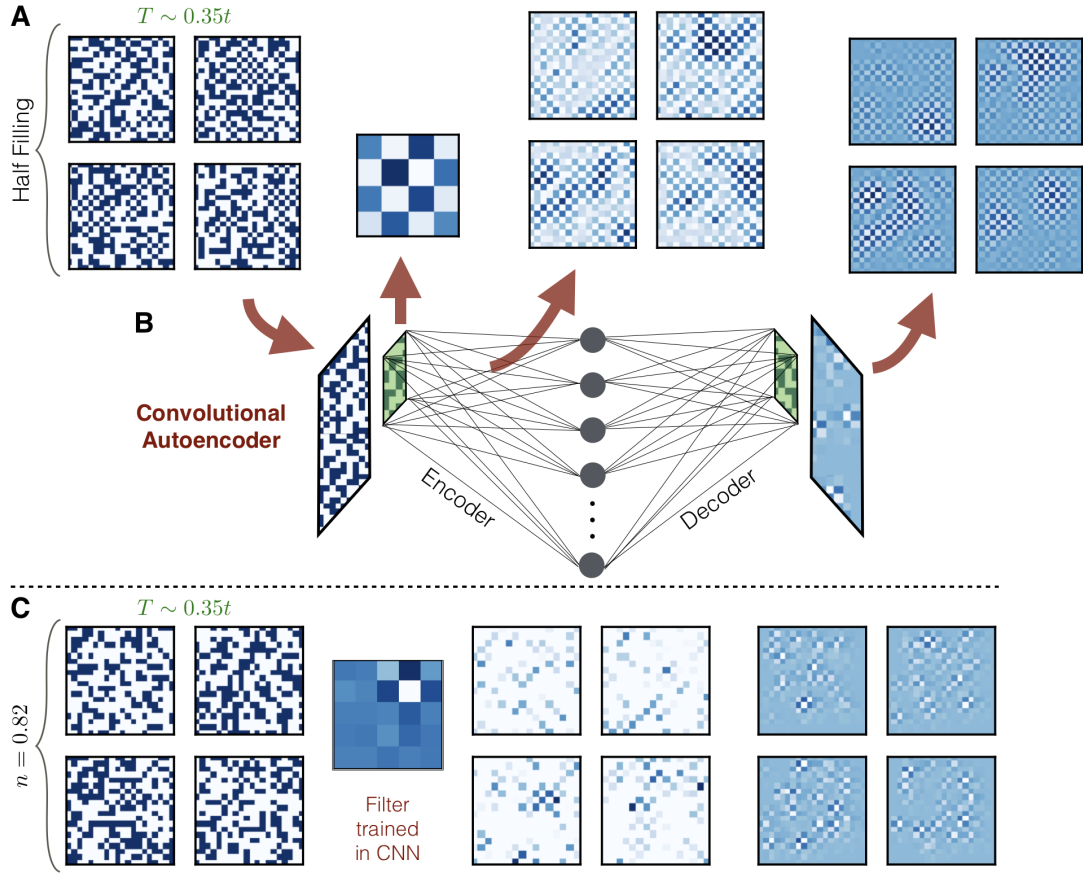


FIG. 15. **Analysis of experimental single-species snapshots using a convolutional autoencoder (CAE).** (A) Input and output of a CAE for $n \sim 1.0$ quantum gas microscope snapshots. Left: Four sample inputs of single-species snapshots at the lowest temperature. Middle left: The filter used in the convolutional layer of the encoder immediately after the input layer. Middle right: Corresponding feature maps from the convolutional layer. Stride of one in each direction has been used. Right: Corresponding snapshots ‘dreamed’ by the CAE. The testing accuracy measured using mean square difference of the input and output is about 77%. (B) The CAE architecture used. The filter of the deconvolution layer of the decoder is chosen to be the same as for the convolution layer, deviating from a true CAE architecture, to further reduce the number of free parameters without compromising the physics. (C) Same as in (A), except that we have used experimental snapshots for $n = 0.82$. We have also used a filter already trained in a CNN (Fig. 2C) since there is a smaller number of snapshots available in this case.

a threshold value for the low/high-temperature snapshots and will be the basis for decision making.

ANALYSIS USING CONVOLUTIONAL AUTOENCODERS

The magnetic correlation for individual snapshots can be highlighted and studied with the use of another artificial neural network architecture known as a convolutional autoencoder (CAE) (Fig. 15B), specifically designed for feature extraction, dimension reduction and regeneration of data without the need to classify. During the training of the CAE, parameters of the network are optimized for the output to be, on average, as close as possible to the input. In general, one can think of the output images as quick impressions, or “dreams”, the neural network has of the input snapshots.

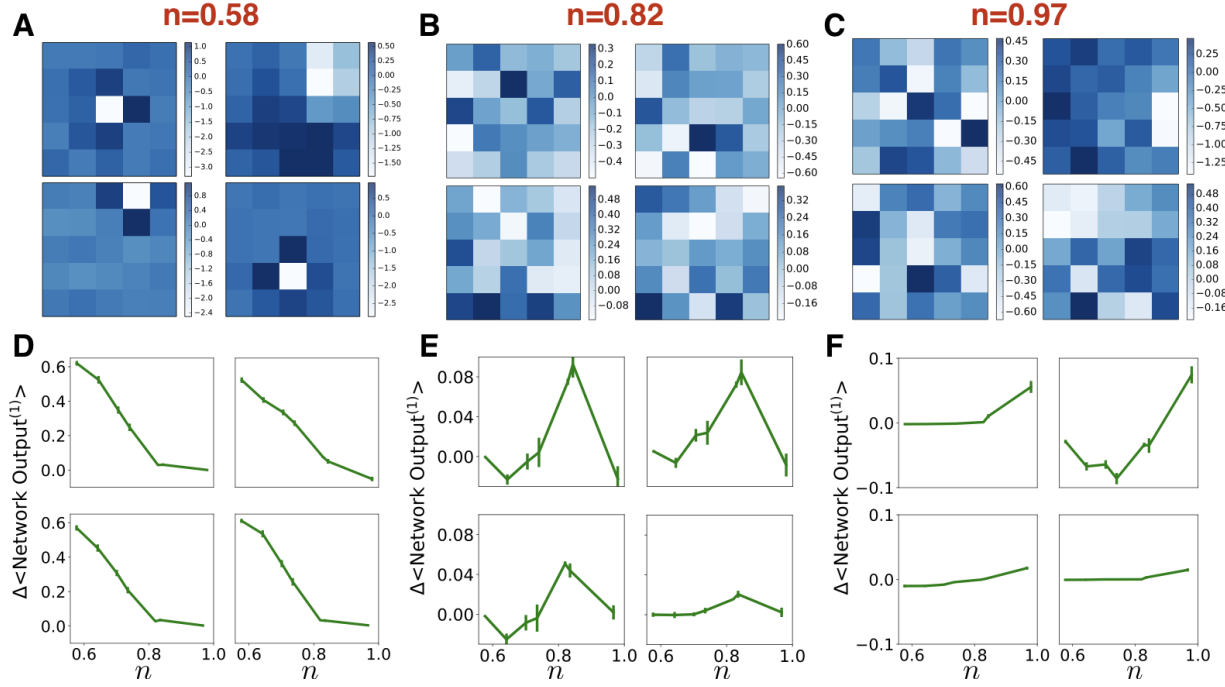


FIG. 16. **Analysis of experimental local moment snapshots at different average densities.** Four independent training runs with the CNN with one filter using low-temperature snapshots at (A) $n = 0.58$, (B) $n = 0.82$, and (C) $n = 0.97$. The testing accuracies are between 85% and 89% for $n = 0.58$, between 60% and 62% for $n = 0.82$, and between 60% and 65% for $n = 0.97$. Similar to Fig. 4B, (D)-(F) show the difference in probabilities that a snapshot and its fake counterpart are categorized by each of the CNNs whose filters are highlighted in (A)-(C) as belonging to the same average density at which the corresponding CNN has been trained.

Figure 15A shows a random sample of four single-species experimental snapshots at half filling at the lowest temperature as inputs along with corresponding outputs of the CAE. The middle panels in the figure show the feature maps corresponding to each of the input snapshots in the left panels. They highlight the important feature promoted by the filter and its distribution by turning all the other seemingly unimportant fluctuations into an average background. Relatively large magnetically ordered domains can be clearly seen for each snapshot. We point out that due to the SU(2) symmetry of the model, AF ordering observed in the projected S_z basis can on average only account for 1/3 of all spin ordering. The same analysis performed using single-species snapshots at $n = 0.82$ demonstrates the depleted nature of the magnetic correlation as a result of doping (Fig. 15C).

TRAINING WITH SNAPSHOTS OF LOCAL MOMENTS

Following Fig. 3 of the main text, in Fig. 16(A)-(C) we show more of the filters trained in the CNN with one filter using experimental snapshots at different average densities. The accuracies are significantly higher at $n = 0.58$, where the nearest-neighbor local moment correlations are the most negative. At $n = 0.82$ and $n = 0.97$, the accuracies are

between 60% and 65% and the filters display more random patterns. Figure 16(D)-(F) show the same quantity as in Fig. 4B of the main text for each of the CNNs whose filters are highlighted in Fig. 16(A)-(C). The maxima around the same density at which the corresponding CNNs have been trained, indicate that patterns found in the filters are most effective in distinguishing correlations between local moments at those densities.

Figure 17 shows the result of training a CNN with sixteen filters using 15000 10×10 theory snapshots of local moments. This is the same CNN whose filters are featured in Fig. 4D of the main text. To obtain the snapshots in the DQMC, we note that for a particular auxiliary field, the expectation value of the local double occupancy reduces to its uncorrelated value; the product of the expectation values for spin-up and spin-down occupancies. Therefore, the local moment at site i can be written as $\langle \hat{n}_{i\uparrow} \rangle + \langle \hat{n}_{i\downarrow} \rangle - 2 \langle \hat{n}_{i\uparrow} \rangle \langle \hat{n}_{i\downarrow} \rangle$, where $\hat{n}_{i\sigma}$ is the density operator for spin- σ at site i .

Figure 17A shows the general improvement of the testing accuracy by increasing the number of filters. Figure 17B shows the sixteen trained filters, which similar to what we find for spin, point to only short-range fluctuations. One can find many redundancies. However, a few representative patterns (those features in Fig. 4D of the main text) emerge. Figure 17C shows the average network output when the network trained at $n = 0.82$ is tested on configurations across a range of densities. We also test the network on fake snapshots. A non-monotonic behavior emerges in both cases. Subtracting the average network output for the real and fake snapshots at each density results in a curve that has a broad peak around $n = 0.85$ and showcases the extent of learned correlations between local moments in this CNN that have to do with factors other than the average density itself (Fig. 17D).

To attribute certain features seen in trained filters in Fig. 17B to correlations unique to the NFL region, we have to rule out their dominance at other densities. Figure 17E shows the performance of individual filters over the same range of densities we used to study the network output. Figure 17F further highlights the values in Fig. 17E at $n = 0.82$. Based on these results, filters that significantly contribute to CNNs' decision making process and are unique to the NFL phase, and therefore, are the best candidates for offering insight into local moment fluctuations are $m = 1, 3, 6, 7$, and 10. The most frequently seen correlation seems to be the one between two neighboring empty sites. This feature, shows up in filters trained on density snapshots too (see below). Filters $m = 6$ and 13 signal that the network also partly uses the information about the density gradient near local moments to make a decision.

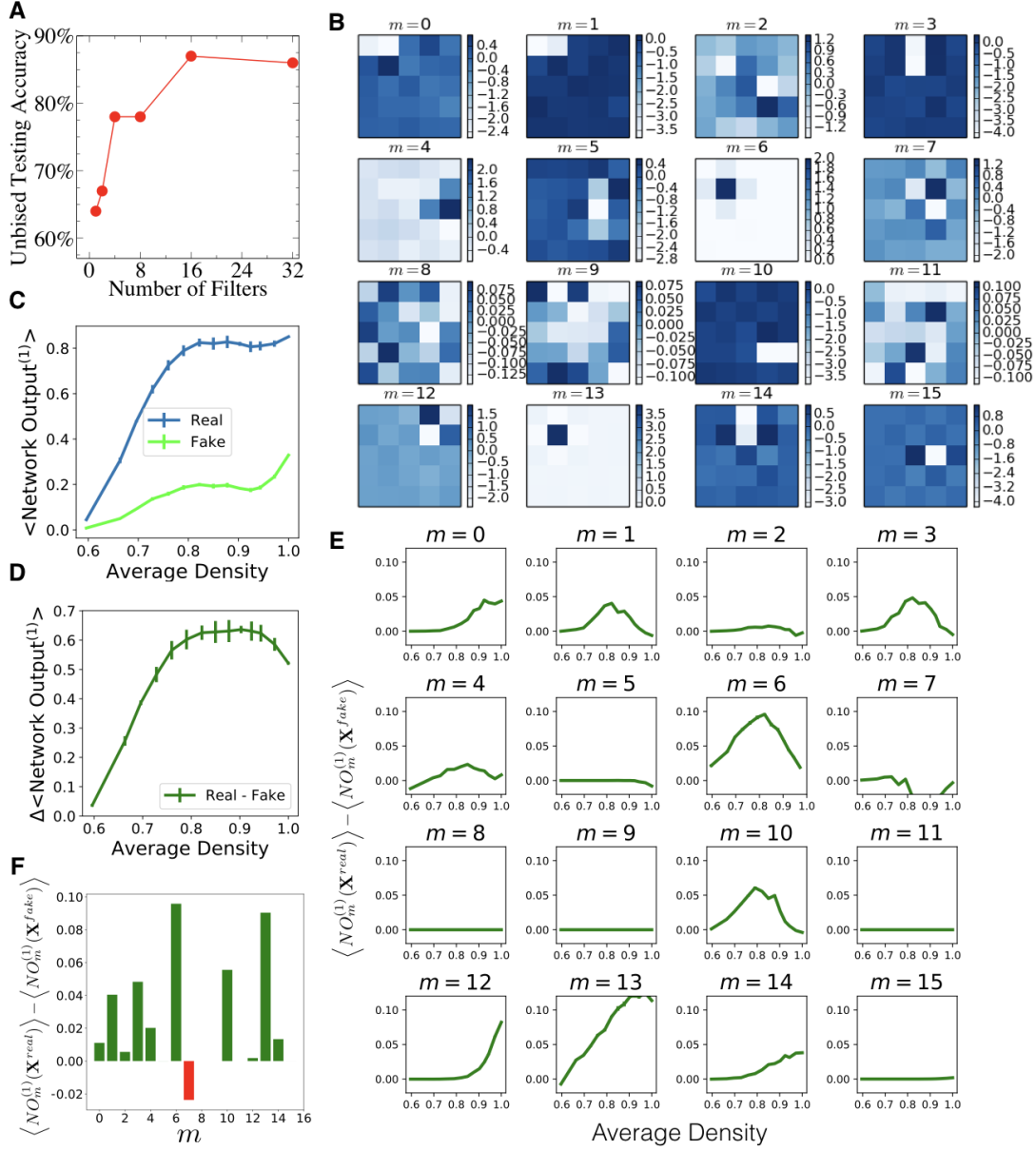


FIG. 17. **Analysis of DQMC local moment snapshots using a CNN with sixteen filters.** (A) The general improvement in the prediction accuracy of the CNN by increasing the number of filters. (B) Trained filters when $n = 0.82$ and $T = 0.44t$. Note that pixel values or their range in one filter should not be compared with those in other filters since a filter-dependent bias is added to the result of the convolution before it is passed through the ReLU activation function (see Eq. 7). The testing accuracy is around 87%. (C) Average network output when a real or fake DQMC snapshot is provided as input, as a function of average density for this CNN. Here, 1 means all the snapshots are classified as likely to be real $n = 0.82$ snapshots, 0 means all the snapshots are classified as likely to be fake $n = 0.82$ snapshots, and 0.5 means neither of the two options is preferred. (D) The difference between the two curves in (C), representing the average percentage the decisions made by the CNN have to do with factors other than the density itself. (E) Similar to (D) when the CNN has access to one filter at a time (see Eq. 8). (F) Same as in (E), but at $n = 0.82$.

TRAINING WITH DQMC SNAPSHOTS OF DENSITY

Sample results for a CNN with sixteen filters trained on full density theory snapshots is shown in Fig. 18. In Fig. 18A, we show the improvement in accuracy as a function of the number of filters when 15,000 or 4,000 snapshots

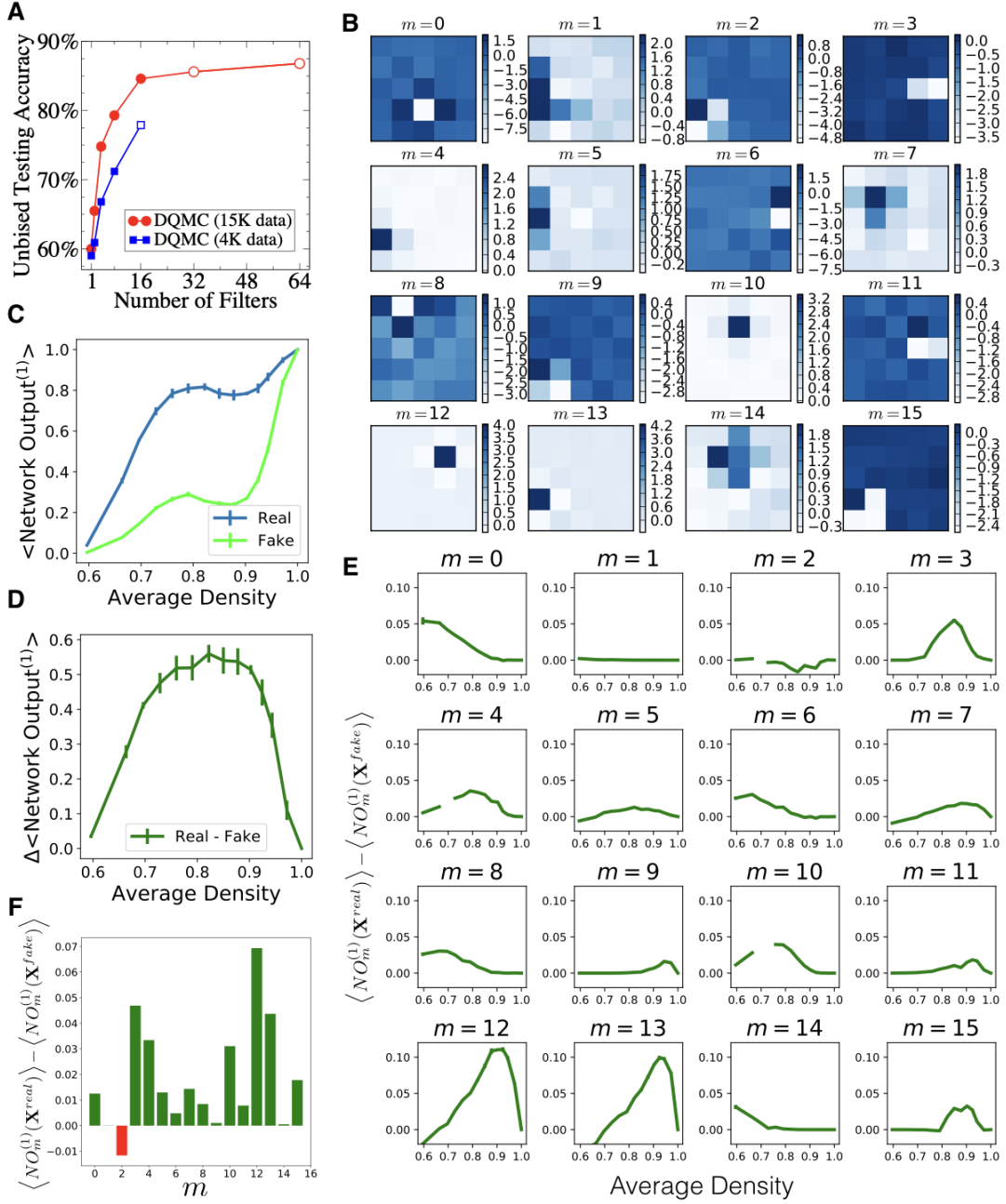


FIG. 18. **Analysis of DQMC density snapshots using a CNN with sixteen filters.** Similar to Figs. 17, but for the case in which the CNN is trained using DQMC full density snapshots.

are used in the training. Remarkably, the unbiased testing accuracy can exceed 85%, however, we encounter signs of overfitting when N_f is increased to 32 for the former or 16 for the latter.

Figures 18B - F show the same quantities as in Fig. 17, but when training with density snapshots. We find that while the shape of the network output vs density in Fig. 18C can vary dramatically from one CNN trained at $n = 0.82$ to the next, the difference shown in Fig. 18D consistently takes a form that can be thought of as a NFL “order

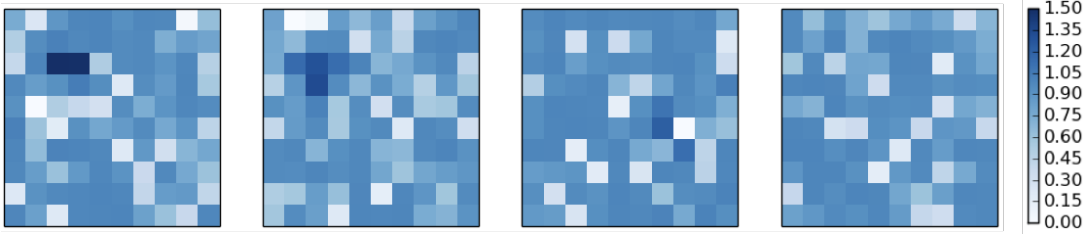


FIG. 19. A sample of DQMC density snapshots in the NFL region yielding the largest network signal in the CNN in Fig. 18 for a real snapshot.

parameter”; a nonlinear function of the density profile represented by the CNN. Testing our CNN on snapshots for different temperatures, U ’s, and system sizes all leads to results consistent with this possibility (see Fig. 20).

Performance of individual filters in Fig. 18E and F shows that most filters likely have an appreciable contribution to the overall network output, with filters $m = 3, 4, 10, 12$ and 13 providing the largest signals. Filter $m = 3$ has a feature resembling those seen in trained filters of the CNN in Fig. 17 measuring the correlation of two neighboring holes. Features seen in $m = 4$ and 5 indicate that the network is also partly using the knowledge of nearest-neighbor density correlations in its decision making process.

In Fig. 19, we show a sample of four density snapshots in the NFL region which are regarded as 100% real by the CNN presented in Fig. 18. It is very hard to discern any patterns with the naked eye using individual snapshots, although some particle-rich and particle-poor regions can be identified in each.

PERFORMANCE OF CNNS ACROSS DENSITIES

To further investigate the trends in the CNN’s signal in the NFL region and what that may teach us about the phase as model parameters change, in Fig. 20, we compare the signal we saw in Fig. 18D to one obtained by testing the same trained CNN with 16 filters on snapshots generated in DQMC under various circumstances. In Fig. 20A, we show that the signal is generally suppressed upon increasing the temperature, which is consistent with correlations being washed away at high temperatures.

We note that in the presence of the fermion “sign problem” [47–49], we treat the network output during the testing process the same way the expectation value of a conventional observable, \hat{O} , is treated and use $\langle \hat{O} \times \text{sgn} \rangle / \langle \text{sgn} \rangle$ in place of $\langle \hat{O} \rangle$, where sgn is the sign associated with the auxiliary field configuration resulting in a snapshot, as the average [11]. This is justified since like many other observables, the network output is simply a nonlinear function of the auxiliary field. Therefore, an exponentially small $\langle \text{sgn} \rangle$ at low temperatures, for large interaction strengths, or

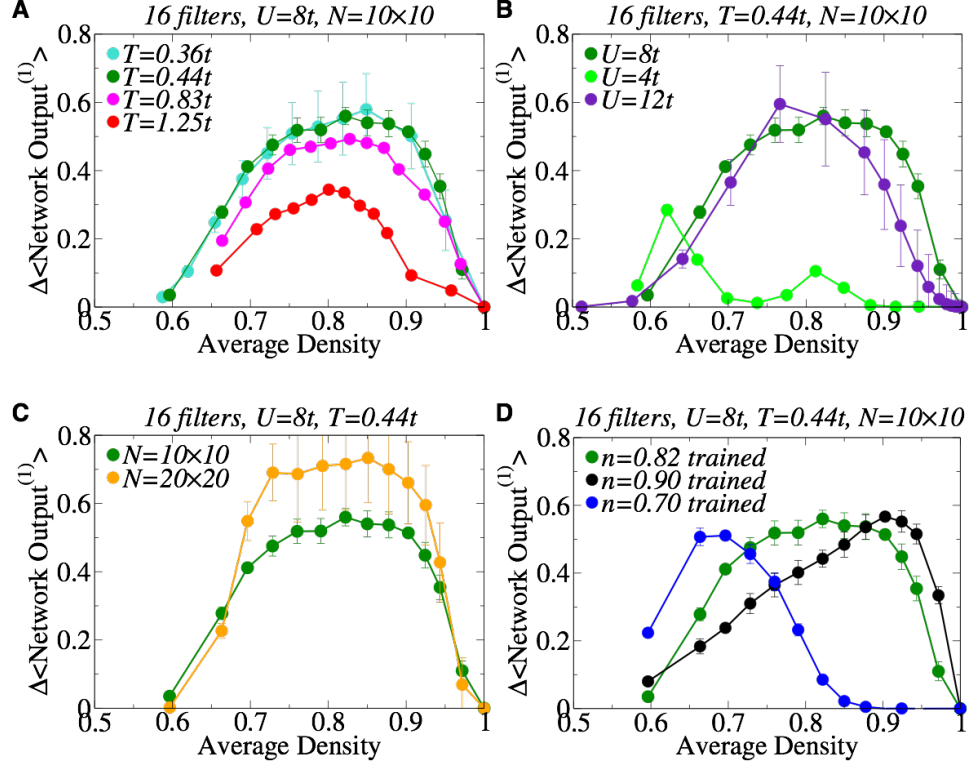


FIG. 20. **Performance of the 16-filter CNNs across densities under various circumstances.** (A) Same as Fig. 18C but testing performed also at other temperatures [the dark green curve in all panels is exactly what is shown in Fig. 18C]. We have used the same 16-filter CNN, trained with data at $n = 0.82$ and $T = 0.44t$, that is featured in Fig. 18. (B) Same as (A), but testing performed at different U 's. (C) Same as (A), but testing performed also on data from a larger $N = 20 \times 20$ cluster. The worst average sign is ~ 0.4 at densities around 0.85, leading to large errorbars (D) Testing results for three different CNNs trained with data at the same $T = 0.44t$ and $U = 8t$, but at different densities.

for larger cluster sizes [49] increases the uncertainty in the average output dramatically and limits our calculations.

In Fig. 20B, we show that a stronger onsite repulsion of $U = 12t$ likely narrows the NFL region of the Hubbard model in the doping space while a weaker interaction of $U = 4t$ seems detrimental to the phase. Figure 20C further shows that charge correlations in fact grow by increasing the system size to 20×20 in the DQMC simulations. Again, the small average sign in this case (~ 0.4) has led to much larger error bars as compared to the 10×10 case. The large number of 20×20 snapshots around $n = 0.82$ with a negative sign and the fact that training neural networks in sign-problematic regions to infer correlations of the Fermi-Hubbard model without a strategy to properly take the sign problem into account is not justified is the reason we have chosen to work mainly with the 10×10 cluster in this study.

Finally, Fig. 20D demonstrates what happens if we trained the same CNN with 16 filters not at $n = 0.82$, but at other average densities. We find that CNNs trained to distinguish real from fake density snapshots in the Fermi liquid region of the model ($n \sim 0.7$) and closer to half filling ($n = 0.9$) show peaks in the respective regions when tested

on snapshots across the range of densities. This makes sense since each CNN is asked to focus on charge correlations specific to the respective regions and not necessarily on those relevant to the NFL phase.
